Title: Photochemical Properties and Structure Characterization of $(BiO)_2CO_3$ Nanowires Doped with Alkaline-earth Metal Ions

Authors: Kuixin Cui, Yuehui He, Yujiao Guo, Shengming Jin

PII: S0025-5408(16)32473-4
DOI: http://dx.doi.org/doi:10.1016/j.materresbull.2017.02.026
Reference: MRB 9172

To appear in: *MRB*

Received date: 13-12-2016
Revised date: 25-1-2017
Accepted date: 15-2-2017

Please cite this article as: Kuixin Cui, Yuehui He, Yujiao Guo, Shengming Jin, Photochemical Properties and Structure Characterization of (BiO)2CO3 Nanowires Doped with Alkaline-earth Metal Ions, Materials Research Bulletin http://dx.doi.org/10.1016/j.materresbull.2017.02.026

Photochemical Properties and Structure Characterization of $(BiO)_2CO_3$ Nanowires Doped with Alkaline-earth Metal Ions

Kuixin Cui[1,2],Yuehui He[1], Yujiao Guo[2], Shengming Jin[2,3]*

1. Powder Metallurgy Research Institute, Central South University, Changsha 410083, P.R. China. E-mail: kxcui2010@csu.edu.cn

2. School of Minerals Processing and Bioengineering, Central South University, Changsha 410083, P.R. China. Fax: +86-731-88710804; Tel: +86-731-88877204; E-mail: shmjin@mail.csu.edu.cn

3. Key Laboratory for Mineral Materials and Application of Hunan Province, Central South University, Changsha 410083, P.R. China.

Graphical abstract

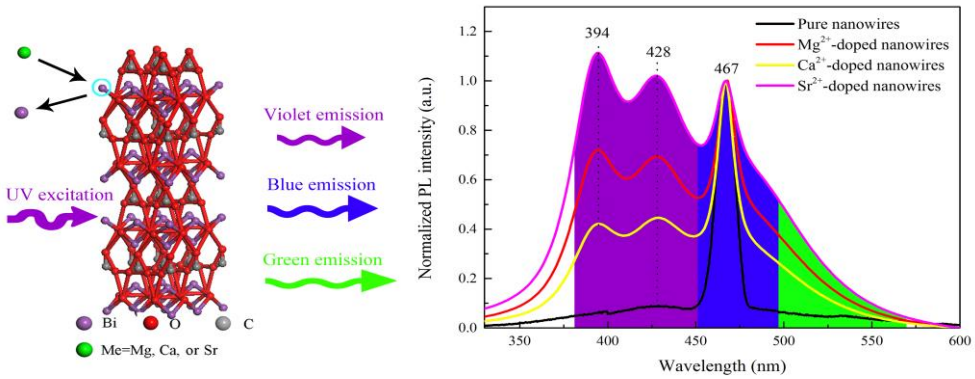

Highlights

- Wire-like $(BiO)_2CO_3$ and alkaline-earth metal ions doped-$(BiO)_2CO_3$ were prepared.
- The cell parameters of doped nanowires shifted from those of pure nanowires.
- TEM images show the doped ions introduced internal defects into $(BiO)_2CO_3$ nanowires.
- Doping ions altered PL emission intensity of $(BiO)_2CO_3$ nanowires.
- Alkaline-earth metal ions doped-$(BiO)_2CO_3$ had enhanced photocatalytic activity.

Abstract

The photoluminescence (PL) properties and photocatalytic activities of pure $(BiO)_2CO_3$ nanowires and $(BiO)_2CO_3$ nanowires doped with alkaline-earth metal ions (Mg^{2+}, Ca^{2+}, and Sr^{2+}) were studied. X-ray diffraction (XRD) studies confirmed that the as-prepared nanowires were orthogonal $(BiO)_2CO_3$ and the calculated cell parameters of alkaline-earth metal ions doped-$(BiO)_2CO_3$ nanowires shifted from those of pure $(BiO)_2CO_3$ nanowires. High-resolution transmission electron microscopy (HRTEM) images demonstrated that numerous defects were introduced into $(BiO)_2CO_3$ nanowires by the doped ions. PL observations showed that $(BiO)_2CO_3$ doping altered the relative intensity of PL emissions, by particularly lowering the emission at 467 nm. The Sr^{2+} ions and Ca^{2+} ions showed the strongest and weakest effect on the PL property of $(BiO)_2CO_3$ nanowires, respectively. The alkaline-earth metal ions doped nanowires had enhanced photocatalytic activities, comparing to the pure nanowires. Therefore, the PL property and photochemical performance of $(BiO)_2CO_3$ nanowires were expected to be adjusted by doping with various cations.

Keywords: Photoluminescence; $(BiO)_2CO_3$ nanowires; alkaline-earth metal; ion-doped $(BiO)_2CO_3$ nanowires; photocatalytic activity

1 Introduction

In recent years, bismuth-containing ternary compounds, such as BiO_xX_y (X=Cl, Br, or I)[1-3], $BiVO_4$[4-6], Bi_2WO_6[7,8], Bi_3NbO_7[9], $BiPO_4$[10], $Bi_6S_2O_{15}$[11], $(BiO)_2CO_3$[12], et al., have attracted a great of attention due to their outstanding properties[13]. Among them, bismuth subcarbonate ($(BiO)_2CO_3$) has become one of the most popular researched semiconductors in the past decade.[14-16] Because of its unique layered structure and tunable band gap, $(BiO)_2CO_3$ has potential applications as photocatalysts[17-19], sensor material[20], anti-bacterial material[14,21] and so on. $(BiO)_2CO_3$ with various morphologies, size, and band gap has been prepared using the hydrothermal treatment or solvothermal method, and its photocatalytic activities were widely studied.[12] However, the photocatalytic efficiency of pure $(BiO)_2CO_3$ remains low because of the broad band gap. The band gap of a semiconductor is determined by its electronic structure and microstructure. Besides, photoluminescence (PL) has been widely used to study the electronic structures, surface defects, photo-induced charge carrier separation and recombination processes of semiconductor nanomaterials because of its non-contact, nondestructive features.[22] Considering doping ions could modify the microstructures, electrical structures, and surface defects of semiconductor materials, $(BiO)_2CO_3$ doped with anions were prepared to improve their performance recently.[23-26] Pure $(BiO)_2CO_3$ microspheres (with a diameter of around 2μm) and CO_3^{2-} self-doped $(BiO)_2CO_3$ microspheres showed a broad PL emission centered at 413 nm after excitation by a 250

nm light. The PL intensity decreased with increasing CO_3^{2-} content, while the photocatalytic activity increased with increasing CO_3^{2-} content.[23] Chang et al. introduced sulfur into $(BiO)_2CO_3$ to form $Bi_2O_2(CO_3)_{1-x}S_x$, and their results showed $Bi_2O_2(CO_3)_{1-x}S_x$ with different sulfur showed different UV-DRS property and photocatalytic activities.[24] N-doped $(BiO)_2CO_3$ microspheres prepared by the hydrothermal method showed enhanced photocatalytic activity towards removal of NO under visible light irradiation.[25,26] However, very little works about the PL properties and photocatalytic activities of cations doped $(BiO)_2CO_3$ were reported. Zhang et al. prepared $(BiO)_2CO_3:Eu^{3+}$ microspheres and studied their PL property using an excitation wavelength of 395 nm, results showed that three emission peaks appeared centering at 560, 592 and 613 nm and all the emission peaks corresponded to the specific emissions of Eu^{3+} ions.[27]

Inspired by the achievements in the cations–doped Bi_2WO_6 photocatalysts[28-30], it has been accepted that cation doping can enhance the photocatalytic activity of the photocatalysts. Alkaline-earth metal ions (Mg^{2+}, Ca^{2+}, and Sr^{2+}) are widely employed as dopants in modifying the electronic structures and properties of semiconductors. Doping Mg into ZnO nanoparticles inhibited the growth of particles size, increased the band gap and enhanced the PL emission.[31] The photocatalytic performance of $BiFeO_3$ nanofibers can be improved by the Ca-doping.[32] Sr-doped CdS–ZnS solid solution photocatalysts showed enhanced photocatalytic activities compared with pure CdS–ZnS photocatalyst because the doping metal ions induced defects, which could improve the separation of the

electrons and holes.[33] It is believed that doping alkaline-earth metal ions (Mg^{2+}, Ca^{2+}, and Sr^{2+}) could modify the PL property of $(BiO)_2CO_3$ and improve the photocatalytic activity. However, to the best of our knowledge, the photochemical properties of alkaline-earth metal ions (Mg^{2+}, Ca^{2+}, and Sr^{2+})-doped $(BiO)_2CO_3$ nanowires have not been reported.

In order to understand the effect of cation-doping on the photochemical properties, it is imperative to carry out systematic analysis on the photochemical properties of $(BiO)_2CO_3$ with alkaline-earth metal ions doping. In this paper, pure $(BiO)_2CO_3$ nanowires and alkaline-earth metal ions (Mg^{2+}, Ca^{2+}, and Sr^{2+}) doped-$(BiO)_2CO_3$ nanowires were prepared by hydrothermal method. The effect of alkaline-earth metal ions (Mg^{2+}, Ca^{2+}, and Sr^{2+}) on the microstructure and PL property of $(BiO)_2CO_3$ nanowires was studied in detail. Moreover, their enhanced photocatalytic activity was demonstrated by the decomposition of xanthate under visible light irradiation.

2 Experimental

2.1 Materials and methods

The bismuth trioxide powders (Bi_2O_3) were purchased from Changde Fine Chemical Co. Ltd. Sodium chloride (NaCl) and sodium carbonate (Na_2CO_3) were bought from Tianjin Kernel Chemical Reagent Co. Ltd. Magnesium chloride ($MgCl_2$), calcium chloride ($CaCl_2$), and strontium chloride ($SrCl_2$) were purchased from Xilong Chemical Co., Ltd. All chemicals were used as they were received and without further purification.

Deionized water was used in the experiments.

In a typical synthesis of Mg^{2+}-doped $(BiO)_2CO_3$ nanowires, 100 mmol NaCl, 0.5 mmol $MgCl_2$ and 5 mmol Na_2CO_3 were first dissolved in 70 mL of deionized water, and the solution was adjusted to pH 3.0 using 1 M HCl. Afterward, 5 mmol Bi_2O_3 was added into the solution under magnetic stirring conditions and kept the stability of pH 3.0. Then, the mixture was transferred into a 100-mL Teflon-lined stainless steel autoclave, stirred magnetically for 6 h at 160 °C, and subsequently cooled to room temperature. Afterward, the products were collected by filtration, washed several times with deionized water and ethanol, and dried overnight in an oven at 60 °C. The procedure for the preparation of Ca^{2+}-doped, and Sr^{2+}-doped $(BiO)_2CO_3$ nanowires were same as that for the preparation of Mg^{2+}-doped nanowires, except for the replacement of the $MgCl_2$ with $CaCl_2$ and $SrCl_2$, respectively.

2.2 Characterization

The phase composition of the as-synthesized $(BiO)_2CO_3$ nanowires was identified by powder X-ray diffractometry (XRD, D/max, Rigaku, Japan) with Cu Kα as a radiation source. The morphology was characterized by scanning electron microscopy (SEM, Quanta 250 FEG, FEI, America), transmission electron microscopy (TEM, JEM-2100F, JEOL, Japan) and high-resolution TEM (HRTEM, JEM-2100F, JEOL, Japan). PL measurement was carried out by a fluorescence spectrometer (FLS980, Edinburgh Instruments, UK) using an excitation wavelength of 250 nm at room temperature. The

photocatalytic activity was evaluated by decomposition of sodium isopropyl xanthate solution under UV-visible light irradiation.

3 Results and Discussion

3.1 XRD characterization

The phase composition of alkaline-earth metal ions doped $(BiO)_2CO_3$ nanowires was analyzed using XRD. Pure $(BiO)_2CO_3$ nanowires were employed for comparison. As shown in Figure 1, all the diffraction peaks of pure $(BiO)_2CO_3$ nanowires could be indexed to the orthorhombic phase with the lattice constants a = 3.865 Å, b = 3.862 Å, and c = 13.675 Å ($(BiO)_2CO_3$, ICDD PDF card No. 09-4740). Most of the diffraction peaks of alkaline-earth metal ions doped $(BiO)_2CO_3$ nanowires could be indexed to the orthorhombic $(BiO)_2CO_3$, and the rest three peaks emerged at 14.9°, 25°, and 29° (2-theta) could be assigned to $BiO_{1.5}$ (ICDD PDF card No. 78-0736). Results apparently indicated that the relative peak intensity varied from each other, intensity ratio of (002) to (013) decreased, whereas the intensity ratio of (110) to (013) increased, suggesting that the doped earth metal ions affected the growth orientation of $(BiO)_2CO_3$ nanowires.

The lattice parameters were calculated based on the XRD patterns to evaluate the effect of dopants on the crystal structure, as listed in Table 1. The ironic radius ratio of M^{2+}/Bi^{3+} (M^{2+} = Mg^{2+}, Ca^{2+}, or Sr^{2+} ion) were also listed in Table 1. Results indicate that the

lattice parameters of as-synthesized pure $(BiO)_2CO_3$ nanowires greatly agree with the standard values. Due to the presence of the doped ions, the lattice parameters of doped nanowires were less than the theoretical lattice parameters, especially for the *c* value. The calculated *c* value of nanowires increased with the sequence, Mg^{2+}-doped $(BiO)_2CO_3$ nanowires < Ca^{2+}-doped $(BiO)_2CO_3$ nanowires < Sr^{2+}-doped $(BiO)_2CO_3$ nanowires after doping with Mg^{2+}, Ca^{2+}, or Sr^{2+}, indicating that doping by ions substituted Bi^{3+} and deformed the structure along *c*-axis to some extent. In particular, the cell parameters of Mg^{2+}-doped $(BiO)_2CO_3$ nanowires were 3.845 × 3.842 × 13.396 Å, which were much smaller than those of pure nanowires and the standard values because of the smaller ionic radius of Mg^{2+} (0.72 Å) than Bi^{3+} (1.03 Å). On the contrary, the increase in *a* and *b* with doping with Sr^{2+} can be attributed to the larger ionic radius of Sr^{2+} (1.18 Å) compared with that of Bi^{3+}.

3.2 SEM and TEM characterizations

In a typical hydrothermal environment, introducing impure ions may affect the crystalline and growth orientation of nanostructures, resulting in different morphologies and properties. As described in previous work, pure $(BiO)_2CO_3$ nanowires with uniform diameter can be prepared using the hydrothermal method (Shown in Figure 2a).[34] SEM images (Figure 2a) shows the disordered wire-like morphology of the pure $(BiO)_2CO_3$, resulting from the random diffusing of ions under the hydrothermal condition. It was different from those orderly ITO nanowires on the surface of a substrate prepared by the

thermal evaporation methodology, which focused on the conductivity and light absorption[35]. Herein, SEM images were used to evaluate the effects of alkaline-earth metal ions on the morphologies of nanowires. As shown in Figure 2, the morphologies of all samples maintained the wire-like 1D structure despite the separate introduction of different alkaline-earth metal ions. In particular, all the Mg^{2+}-doped, Ca^{2+}-doped, and Sr^{2+}-doped $(BiO)_2CO_3$ nanowires showed several nanowires that were bonded together with some nanosheets. Besides, the ratio of wire-like structure to sheet-like structure differed, which was probably caused by the different ionic radii. The radius of Mg^{2+} is 0.72 Å, which is much smaller than the 1.03 Å radius of Bi^{3+}. Thus, more sheet-like structures appeared, as shown in Figure 2a. In contrast, fewer sheet-like nanostructures emerged in the Sr^{2+}-doped system, and nearly no sheet-like nanostructures could be observed in the Ca^{2+}-doped system due to their similar ionic radius (1.00 Å for Ca^{2+} and 1.18 Å for Sr^{2+}). In other words, the ionic radius of introduced ions affected the formation of nanowires during the hydrothermal treatment of Bi_2O_3, wherein increased mismatch between the added ions and bismuth ions, resulted in the appearance of a more sheet-like nanostructure.

TEM and HRTEM images of Mg^{2+}-doped, Ca^{+}-doped, and Sr^{2+}-doped nanowires were recorded to investigate how the doped ions affected the microstructure of $(BiO)_2CO_3$ nanowires. As a comparison, TEM and HRTEM images of the pure $(BiO)_2CO_3$ nanowires were shown in Figure 3a,3b, which grew along the *b* axis. Figures 3c and 3d show us the TEM and HRTEM images of Mg^{2+}-doped nanowires. It could be

seen that the Mg^{2+}-doped nanowires had diameters about 30 nm and a smooth surface. Clear crystal fringes appeared in the HRTEM image. The spacing of adjacent fringes was measured to be 0.1925 nm, which could be ascribed to (020) plane of $(BiO)_2CO_3$. It indicated that Mg^{2+}-doped $(BiO)_2CO_3$ nanowires grew along the *b* axis, just like pure $(BiO)_2CO_3$ nanowires. According to Figure S1, Bi-O bonds expose on the surface of $(BiO)_2CO_3$ nanowires when they grew along the *b* axis, so it was easy to substitute Bi atom in the Bi-O layers of $(BiO)_2CO_3$ cells. As a result, the original Bi-O tetrahedrons collapsed when smaller ions like Mg^{2+} located at the Bi lattice sites. Numerous distortions could also be observed in the HRTEM image (shown as oval-shaped circles in Fig. 3d). Combining the smaller measured d-value of (020) crystal plane and defects with the XRD results, we concluded that Mg^{2+} intruded upon the original cell of $(BiO_2)CO_3$ resulting in a distorted cell. Figures 3e and 3f show the TEM and HRTEM images of Ca^{2+}-doped nanowires, respectively. The observed nanowires showed a more uniform diameter of 20 nm or so. In Figure 3f, clearer crystal fringes and fewer defects could be observed, comparing with that of Mg^{2+}-doped nanowires. The spacing was measured to be 0.1935 nm, which belonged to the (020) crystal planes, too. Similarly, some defects existed on the surface of the nanowire because Sr^{2+} ions substituted some Bi^{3+} ions in the $(BiO)_2CO_3$ nanowires (Figure 3h). Combining HRTEM analysis (enlarged d-spacing and defects) with XRD results, Sr^{2+} was successfully introduced into the $(BiO)_2CO_3$ crystal cell.

3.3 PL properties

The photoluminescence spectra of the as-prepared pure, Mg^{2+}, Ca^{2+}, and Sr^{2+}-doped $(BiO)_2CO_3$ nanowires were recorded at an exciting wavelength of 250 nm. For a better comparison, all the spectra were normalized based on the emission peak at 467 nm, as shown in Figure 4. The pure $(BiO)_2CO_3$ nanowires showed one sharp emission peak at 467 nm, and one weak broad emission region around 425 nm. The peak at 467 nm could be ascribed to the surface defect-induced emission due to the high activity of surface atoms (Bi atoms and O atoms) in $(BiO)_2CO_3$ nanowires, and the weak broad peak around 425 nm could be contributed to the intrinsic defect-induced emission. Oxygen vacancies are the main defect in metal oxidant semiconductors, such as ZnO[36], TiO_2[37], et al. For the $(BiO)_2CO_3$ nanowires, Bi-O layers expose on the surface, which could also lead to oxygen vacancies. These oxygen vacancies acted as recombination centers to show up the 467 nm emission peak in the PL spectrum. Compared to the PL spectrum of pure $(BiO)_2CO_3$ nanowires, the surface defect-induced emission peak at 467 nm appeared broader with a tail. At the same time, the intrinsic emission of $(BiO)_2CO_3$ at 394 nm showed up, indicating the energy band structure and defect types of $(BiO)_2CO_3$ varied from that of pure $(BiO)_2CO_3$ nanowires after doping with alkaline-earth metal ions. Moreover, the intrinsic defect-induced emission peaks shifted to 428 nm in the PL spectra of doped $(BiO)_2CO_3$ nanowires comparing with that of pure nanowires, suggesting that doping alkaline-earth metal ions subtly altered the defect type. The generated Me-O

bonds are ionic bonds rather than covalent bonds of Bi-O because the electronegativities of alkaline-earth metal ions are smaller than that of bismuth ion. As a result, the electron cloud distribution and electronic structure of alkaline-earth metal ions doped-$(BiO)_2CO_3$ nanowires varied from that of pure $(BiO)_2CO_3$ nanowires, leading to the broadened defect-induced PL emission with a tail.[38, 39] It also could be observed that all the PL emission peaks were located at same wavelength positions. Generally, a shift of the PL emission peak occurs after the impure ions are doped in the crystal due to the energy level splitting. However, no noticeable difference in the PL emission positions was observed here, just like the PL features of Mg^{2+}, Ca^{2+}, and Sr^{2+} doped ZnO nanoparticles.[40] Further study is necessary to figure out the likely reasons. In order to have a better understanding of the PL properties, we fitted all the PL spectra based on Gaussian-Lorentz (20:80) calculation. A good fit with four emission peaks centered at 394, 428, 467 and 482 nm was obtained for all of the PL spectra of the samples.

Table 2 shows PL intensity ratio of different chromophores to the total PL emission intensity of pure nanowires and alkaline-earth metal ions-doped $(BiO)_2CO_3$ nanowires based on the Gaussian-Lorentz simulation. The surface defect-induced PL emission made up about 83.53% of the total PL emission, intrinsic defect-induced PL emission (9.63%) and intrinsic PL emission (6.84%). For the Mg^{2+}, Ca^{2+}, and Sr^{2+}-doped $(BiO)_2CO_3$ nanowires, the relative intensity of surface defect-induced emission dropped dramatically, and the impurity defect-induced emissions at 482 nm were dominant because doping with

nonequivalent ions caused numerous impurity defects, which were different from that of pure $(BiO)_2CO_3$ nanowires. The highest intensity of surface defect-induced emission (14.68%) belonged to Ca^{2+}-doped nanowires, followed by 8.87% of Mg^{2+}-doped nanowires, and 4.91% of Sr^{2+}-doped nanowires. The electronegativity of Mg, Ca, Sr, Bi, and O is 1.31, 1.0, 0.95, 2.02, and 3.44,[41] respectively. While the ionic radius of Mg, Ca, Sr, and Bi is 0.72, 1.0, 1.18 Å, and 1.03 for Mg^{2+}, Ca^{2+}, Sr^{2+} , and Bi^{3+} ions[41], respectively. For the geometrical part, the radius of Ca^{2+} is extremely close to that of Bi^{3+}, leading to a minimal structure change in the original crystalline cell of $(BiO)_2CO_3$. Given that the ionic radius of Sr^{2+} was a little bigger than that of Bi^{3+}, the intruded Sr^{2+} could enlarge the original cell of $(BiO)_2CO_3$ and change the surface defect emission, leading to the lowest surface defect-induced PL intensity. The radius of Mg^{2+} was much smaller than that of Bi^{3+}, the ions intruded into $(BiO)_2CO_3$ cells and resulted in shrunken crystal cells and impurity defects. For the $(BiO)_2CO_3$ electronic structural part, the generated Me-O bonds have a different strength after they replaced Bi in the crystal lattice. Based on the electronegativity, the ionicity of an A-B bond is given by[42]:

$$f_{ionic}=1-\exp[-(X_A-X_B)^2/4]$$

Where X_A and X_B are the electronegativities of the elements A and B. So that the ratio of the ionic bond is 0.678, 0.774, 0.787, and 0.396 in Mg-O, Ca-O, Sr-O and Bi-O bond, respectively. The Bi-O bond is more covalent character than ionic character; meanwhile, all the Me-O bonds are ionic bonds. The greater the difference in electronegativity between Me and O, the stronger the ionic bond that will be formed between them. Hence,

the strength of the Me-O bond increase as the following order: Bi-O<Mg-O<Ca-O<Sr-O. After Me had replaced Bi in the crystal lattice, the electron distribution between Me and O shifted from the Bi-O bond, resulting in the shifting of the electronic structure of the doped $(BiO)_2CO_3$ nanowires. Given that both the ionic radius and electronegativity of doped alkaline-earth metal ions are different, the as-obtained PL results reflected the interaction of ionic radius and electronegativity of doped ions. Therefore, doping with alkaline-earth metal ions has a significant effect on the intrinsic defect PL emission and impurity defect PL emission, but has little effect on the intrinsic PL emission of $(BiO)_2CO_3$ nanowires.

3.4 Photocatalytic activity

The enhanced photocatalytic activity of Mg^{2+}, Ca^{2+}, and Sr^{2+}-doped nanowires was determined by degradation of sodium isopropyl xanthate in aqueous solution under UV-visible irradiation using a 250 W mercury lamp as light source. As well, pure $(BiO)_2CO_3$ nanowires were employed as a contrast. Figure 5 shows the plot of degradation rate $(A_0-A_t)/A_0\%)$ of xanthate at different reaction time using Mg^{2+}, Ca^{2+}, Sr^{2+}-doped nanowires and pure $(BiO)_2CO_3$ nanowires as photocatalysts. Here, A_0 is the initial absorbance of sodium isopropyl xanthate, and A_t is the absorbance of sodium isopropyl xanthate solution at a reaction time t. As shown in figure 5, the degradation rate of sodium isopropyl xanthate was less than 5% without photocatalyst. As a contrast, the xanthate was degraded very quickly once the photocatalysts were added into the xanthate

solution. At a time of 30 min without light irradiation, the degradation rate of xanthate by Mg^{2+}, Ca^{2+}, and Sr^{2+}-doped nanowires and pure nanowires was 97.9%, 66.7%, 88.9%, and 52.4%, respectively. The results of UV-vis spectra of the xanthate-containing solution indicated that sodium isopropyl xanthate decomposed into CS_2 and C_3H_7OH under UV-vis irradiation, which was in accordance with the previous results of pure $(BiO)_2CO_3$ nanowires.[29] It might be caused by the different morphologies shown in Figure 2. Mg^{2+}-doped nanowires and Sr^{2+}-doped nanowires contained lots of sheet-like nanostructures, which might absorb xanthate quicker than the single wire-like nanostructure. The decomposition rate increased with the increasing of the reaction time. After 60 min of reaction, the degradation rate of xanthate was 98.9%, 98.5%, 95.9%, and 94.4% in the presence of Mg^{2+}-doped, Ca^{2+}-doped, Sr^{2+}-doped nanowires, and pure nanowires, respectively. The Mg^{2+}-doped-nanowires showed the highest photocatalytic activity, followed by Sr^{2+}-doped nanowires, Ca^{2+}-doped nanowires and pure nanowires, which was in accordance with the PL results. The ions-doped nanowires also showed a high stability of photocatalytic activity after three successive runs (Shown in Fig.S2).

4 Conclusions

In summary, pure and alkaline-earth metal ions (Mg^{2+}, Ca^{2+}, and Sr^{2+})-doped $(BiO)_2CO_3$ nanowires were successfully prepared using the hydrothermal method. The XRD results confirmed that the as-prepared nanowires were of orthogonal $(BiO)_2CO_3$, and the calculated cell parameters of doped-$(BiO)_2CO_3$ nanowires shifted from those of pure

$(BiO)_2CO_3$ nanowires because of the mismatched radii and valence between doped ions and Bi^{3+}. HRTEM images also demonstrated that numerous defects were introduced into the $(BiO)_2CO_3$ nanowires by the doped ions. PL studies showed that the pure $(BiO)_2CO_3$ nanowires displayed one sharp emission at 467 nm, which was caused by surface defects. Doping of $(BiO)_2CO_3$ altered the PL emission relative intensity. The Ca^{2+}-doped $(BiO)_2CO_3$ nanowires showed the similar PL property of pure $(BiO)_2CO_3$ nanowires, followed by Mg^{2+}-doped $(BiO)_2CO_3$ nanowires, and Sr^{2+}-doped $(BiO)_2CO_3$ nanowires, resulting from their different ionic radius and electronegativity. The closer of the radii between the doping atom and Bi atom is, the more similar the PL spectrum of $(BiO)_2CO_3$ nanowires. The photocatalytic activity test demonstrated all the alkaline-earth metal ions doped nanowires had an enhanced photocatalytic activity compared to the pure nanowires. Therefore, the PL emission and photocatalytic activity of $(BiO)_2CO_3$ could be adjusted by adding different impurities.

References

(1) Li, J.; Zhang, L.; Li, Y.; Yu, Y., Synthesis and Internal Electric Field Dependent Photoreactivity of Bi_3O_4Cl Single-Crystalline Nanosheets with High {001} Facet Exposure Percentages. *Nanoscale* **2014**, 167-171.

(2) Kim, W. J.; Pradhan, D.; Min, B.; Sohn, Y., Adsorption/Photocatalytic Activity and Fundamental Natures of BiOCl and BiOClxI1−X Prepared in Water and Ethylene

Glycol Environments, and Ag and Au-doping Effects. *Appl. Catal. B* **2014**, *147*, 711-725.

(3) Lin, X.; Huang, T.; Huang, F.; Wang, W.; Shi, J., Photocatalytic Activity of a Bi-based Oxychloride Bi_3O_4Cl. *J. Phys. Chem. B* **2006**, *110*, 24629-24634.

(4) Tan, H. L.; Wen, X.; Amal, R.; Ng, Y. H., $BiVO_4$ {010} and {110} Relative Exposure Extent: Governing Factor of Surface Charge Population and Photocatalytic Activity. *J. Phys. Chem. Lett.* **2016**, *7*, 1400-1405.

(5) Xiao, Q.; Gao, L.; Zhang, X., Synthesis and Characterization of Highly Visible-Light Active Monoclinic Mesoporous $BiVO_4$. *J. Inorg. Mater.* **2011**, 1256-1260.

(6) Wang, M.; Xi, X.; Gong, C.; Zhang, X. L.; Fan, G., Open Porous $BiVO_4$ Nanomaterials: Electronspinning Fabrication and Enhanced Visible Light Photocatalytic Activity. *Mater. Res. Bull.* **2016**, *74*, 258-264.

(7) Zhang, G.; Lü, F.; Li, M.; Yang, J.; Zhang, X.; Huang, B., Synthesis of Nanometer Bi_2WO_6 Synthesized by Sol–Gel Method and its Visible-Light Photocatalytic Activity for Degradation of 4BS. *J. Phys. Chem. Solids* **2010**, *71*, 579-582.

(8) Xu, X.; Ge, Y.; Wang, H.; Li, B.; Yu, L.; Liang, Y.; Chen, K.; Wang, F., Sol–Gel Synthesis and Enhanced Photocatalytic Activity of Doped Bismuth Tungsten Oxide Composite. *Mater. Res. Bull.* **2016**, *73*, 385-393.

(9) Zhang, G.; Yang, J.; Zhang, S.; Xiong, Q.; Huang, B.; Wang, J.; Gong, W., Preparation of Nanosized Bi_3NbO_7 and its Visible-Light Photocatalytic Property. *J. Hazard. Mater.* **2009**, *172*, 986-992.

(10) Xue, F.; Li, H.; Zhu, Y.; Xiong, S.; Zhang, X.; Wang, T.; Liang, X.; Qian, Y.,

Solvothermal Synthesis and Photoluminescence Properties of $BiPO_4$ Nano-Cocoons and Nanorods with Different Phases. *J. Solid State Chem.* **2009**, *182*, 1396-1400.

(11) Zhou, Y.; Grunwaldt, J.; Krumeich, F.; Zheng, K.; Chen, G.; Stötzel, J.; Frahm, R.; Patzke, G. R., Hydrothermal Synthesis of $Bi_6S_2O_{15}$ Nanowires Structural, in situ EXAFS, and Humidity-Sensing Studies. *Small* **2010**, *6*, 1173-1179.

(12) Selvamani, T.; Asiri, A. M.; Al-Youbi, A. O.; Anandan, S., Emergent Synthesis of Bismuth Subcarbonate Nanomaterials with Various Morphologies Towards Photocatalytic Activities - an Overview. *Mater. Sci. Forum* **2013**, *764*, 169-193.

(13) Zhao, H.; Tian, F.; Wang, R.; Chen, R., A Review On Bismuth-Related Nanomaterials for Photocatalysis. *Rev. Adv. Sci. Eng.* **2014**, *3*, 3-27.

(14) Chen, R.; So, M. H.; Yang, J.; Deng, F.; Che, C.; Sun, H., Fabrication of Bismuth Subcarbonate Nanotube Arrays From Bismuth Citrate. Chem. Commun. 2006, 2265-2267.

(15) Liu, Y.; Wang, Z.; Huang, B.; Yang, K.; Zhang, X.; Qin, X.; Dai, Y., Preparation, Electronic Structure, and Photocatalytic Properties ofPreparation, Electronic Structure, and Photocatalytic Properties of $Bi_2O_2CO_3$ Nanosheet. *Appl. Surf. Sci.* **2010**, *257*, 172-175.

(16) Huang, H.; Wang, J.; Dong, F.; Guo, Y.; Tian, N.; Zhang, Y.; Zhang, T., Highly Efficient $Bi_2O_2CO_3$ Single-Crystal Lamellas with Dominantly Exposed {001} Facets. *Cryst. Growth Des.* **2015**, *15*, 534-537.

(17) Dong, F.; Lee, S. C.; Wu, Z.; Huang, Y.; Fu, M.; Ho, W.; Zou, S.; Wang, B.,

Rose-Like Monodisperse Bismuth Subcarbonate Hierarchical Hollow Microspheres: One-Pot Template-Free Fabrication and Excellent Visible Light Photocatalytic Activity and Photochemical Stability for NO Removal in Indoor Air. *J. Hazard. Mater.* **2011**, *195*, 346-354.

(18) Zhao, T.; Zai, J.; Xu, M.; Zhou, Q.; Su, Y.; Wang, K.; Qian, X., Hierarchical $Bi_2O_2CO_3$ Microspheres with Improved Visible-Light-Driven Photocatalytic Activity. *CrystEngComm* **2011**, *13*, 4010-4017.

(19) Peng, S.; Li, L.; Tan, H.; Wu, Y.; Cai, R.; Yu, H.; Huang, X.; Zhu, P.; Ramakrishna, S.; Srinivasan, M.; Yan, Q., Monodispersed Ag Nanoparticles Loaded On the PVP-assisted Synthetic $Bi_2O_2CO_3$ Microspheres with Enhanced Photocatalytic and Supercapacitive Performances. *J. Mater. Chem. A* **2013**, *1*, 7630-7638.

(20) Zhou, Y.; Wang, H.; Sheng, M.; Zhang, Q.; Zhao, Z.; Lin, Y.; Liu, H.; Patzke, G. R., Environmentally Friendly Room Temperature Synthesis and Humidity Sensing Applications of Nanostructured $Bi_2O_2CO_3$. *Sens. Actuators B-Chem.* **2013**, *188*, 1312-1318.

(21) Qin, F.; Li, G.; Wang, R.; Wu, J.; Sun, H.; Chen, R., Template-Free Fabrication of Bi_2O_3 and $(BiO)_2CO_3$ Nanotubes and their Application in Water Treatment. *Chem. Eur. J.* **2012**, *18*, 16491-16497.

(22) Gilliland, G. D., Photoluminescence Spectroscopy of Crystalline Semiconductors. *Mater. Sci. Eng. R-Rep.* **1997**, *18*, 99-399.

(23) Huang, H.; Li, X.; Wang, J.; Dong, F.; Chu, P. K.; Zhang, T.; Zhang, Y.,

Anionic Group Self-Doping as a Promising Strategy: Band-Gap Engineering and Multi-Functional Applications of High-Performance CO_3^{2-}-Doped $Bi_2O_2CO_3$. *ACS Catal.* **2015**, *5*, 4094-4103.

(24) Chang, C.; Teng, F.; Liu, Z., Fully Understanding the Photochemical Properties of $Bi_2O_2(CO_3)_{1-x}S_x$ Nanosheets. *Langmuir* **2016**, *32*, 3811-3819.

(25) Dong, F.; Xiong, T.; Zhao, Z.; Sun, Y.; Fu, M., Ammonia Induced Formation of N-doped $(BiO)_2CO_3$ Hierarchical Microspheres: The Effect of Hydrothermal Temperature On the Morphology and Photocatalytic Activity. *CrystEngComm* **2013**, *15*, 10522-10532.

(26) Dong, F.; Sun, Y.; Fu, M.; Ho, W.; Lee, S. C.; Wu, Z., Novel in Situ N-Doped $(BiO)_2CO_3$ Hierarchical Microspheres Self-Assembled by Nanosheets as Efficient and Durable Visible Light Driven Photocatalyst. *Langmuir* **2012**, *28*, 766-773.

(27) Zhang, N.; Xiong, H.; Liu, Y.; Li, R.; Leng, Z.; Gan, S., Novel Synthesis Route to Uniform Nanosheet $Bi_2O_2CO_3$:Eu^{3+} Crystals with Luminescence Properties. *Appl. Surf. Sci.* **2015**, *357*, 255-261.

(28) Song, X. C.; Zheng, Y. F.; Ma, R.; Zhang, Y. Y.; Yin, H. Y., Photocatalytic Activities of Mo-doped Bi_2WO_6 Three-Dimensional Hierarchical Microspheres. *J. Hazard. Mater.* **2011**.

(29) Guo, S.; Li, X.; Wang, H.; Dong, F.; Wu, Z., Fe-Ions Modified Mesoporous Bi_2WO_6 Nanosheets with High Visible Light Photocatalytic Activity. *J. Colloid Interf. Sci.* **2012**, *369*, 373-380.

(30) Li, W. T.; Huang, W. Z.; Zhou, H.; Yin, H. Y.; Zheng, Y. F.; Song, X. C., Synthesis and Photoactivity Enhancement of Ba Doped Bi_2WO_6 Photocatalyst. *Mater. Res. Bull.* **2015**, *64*, 432-437.

(31) Arshad, M.; Meenhaz Ansari, M.; Ahmed, A. S.; Tripathi, P.; Ashraf, S. S. Z.; Naqvi, A. H.; Azam, A., Band Gap Engineering and Enhanced Photoluminescence of Mg Doped ZnO Nanoparticles Synthesized by Wet Chemical Route. *J. Lumin.* **2015**, *161*, 275-280.

(32) Feng, Y.; Wang, H.; Luo, Y.; Shen, Y.; Lin, Y., Ferromagnetic and Photocatalytic Behaviors Observed in Ca-doped $BiFeO_3$ Nanofibres. *J. Appl. Phys.* **2013**, *113*, 146101.

(33) Zhang, K.; Jing, D.; Chen, Q.; Guo, L., Influence of Sr-doping On the Photocatalytic Activities of CdS–ZnS Solid Solution Photocatalysts. *Int. J. Hydrogen Energ.* **2010**, *35*, 2048-2057.

(34) Cui, K.; He, Y.; Jin, S., Enhanced UV–Visible Response of Bismuth Subcarbonate Nanowires for Degradation of Xanthate and Photocatalytic Reaction Mechanism. *Chemosphere* **2016**, *149*, 245-253.

(35) Li, L.; Chen, S.; Kim, J.; Xu, C.; Zhao, Y.; Ziegler, K. J., Controlled Synthesis of Tin-Doped Indium Oxide (ITO) Nanowires. *J. Cryst. Growth* **2015**, *413*, 31-36.

(36) Zeng, H.; Duan, G.; Li, Y.; Yang, S.; Xu, X.; Cai, W., Blue Luminescence of ZnO Nanoparticles Based on Non-Equilibrium Processes: Defect Origins and Emission Controls. *Adv. Funct. Mater.* **2010**, *20*, 561-572.

(37) Nowotny, M. K.; Sheppard, L. R.; Bak, T.; Nowotny, J., Defect Chemistry of

Titanium Dioxide. Application of Defect Engineering in Processing of TiO_2-Based Photocatalysts. *J. Phys. Chem. C.* **2008**, *112*, 5275-5300.

(38) Schubert, E. F.; Goepfert, I. D.; Grieshaber, W.; Redwing, J. M., Optical Properties of Si-doped GaN. *Appl. Phys. Lett.* 1997, *71*, 921-923.

(39) Qu, S. C.; Zhou, W. H.; Liu, F. Q.; Chen, N. F.; Wang, Z. G., Photoluminescence Properties of Eu^{3+}-Doped ZnS Nanocrystals Prepared in a Water/Methanol Solution. *Appl. Phys. Lett.* 2002, *80*.

(40) Haja Hameed, A. S.; Karthikeyan, C.; Sasikumar, S.; Senthil Kumar, V.; Kumaresan, S.; Ravi, G., Impact of Alkaline Metal Ions Mg^{2+}, Ca^{2+}, Sr^{2+} and Ba^{2+} On the Structural, Optical, Thermal and Antibacterial Properties of ZnO Nanoparticles Prepared by the Co-Precipitation Method. *J. Mater. Chem. B* **2013**, *1*, 5950.

(41) Pauling L., *The Nature of the Chemical Bond*, Cornell Univ., USA, 3rd ed., **1960**.

(42) Phillips, J. C., *Bonds and Bands in Semicondutors*; Academic Press: New York and London, 1973.

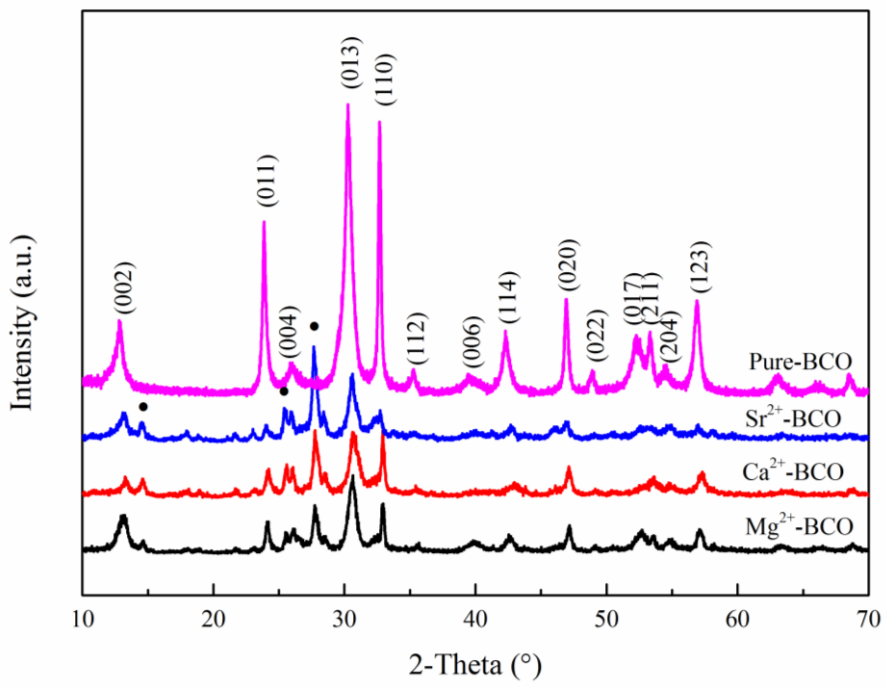

Figure 1. XRD patterns of Mg^{2+}-doped, Ca^{2+}-doped, and Sr^{2+}-doped $(BiO)_2CO_3$ nanowires and pure $(BiO)_2CO_3$ nanowires (solid circles: $BiO_{1.5}$).

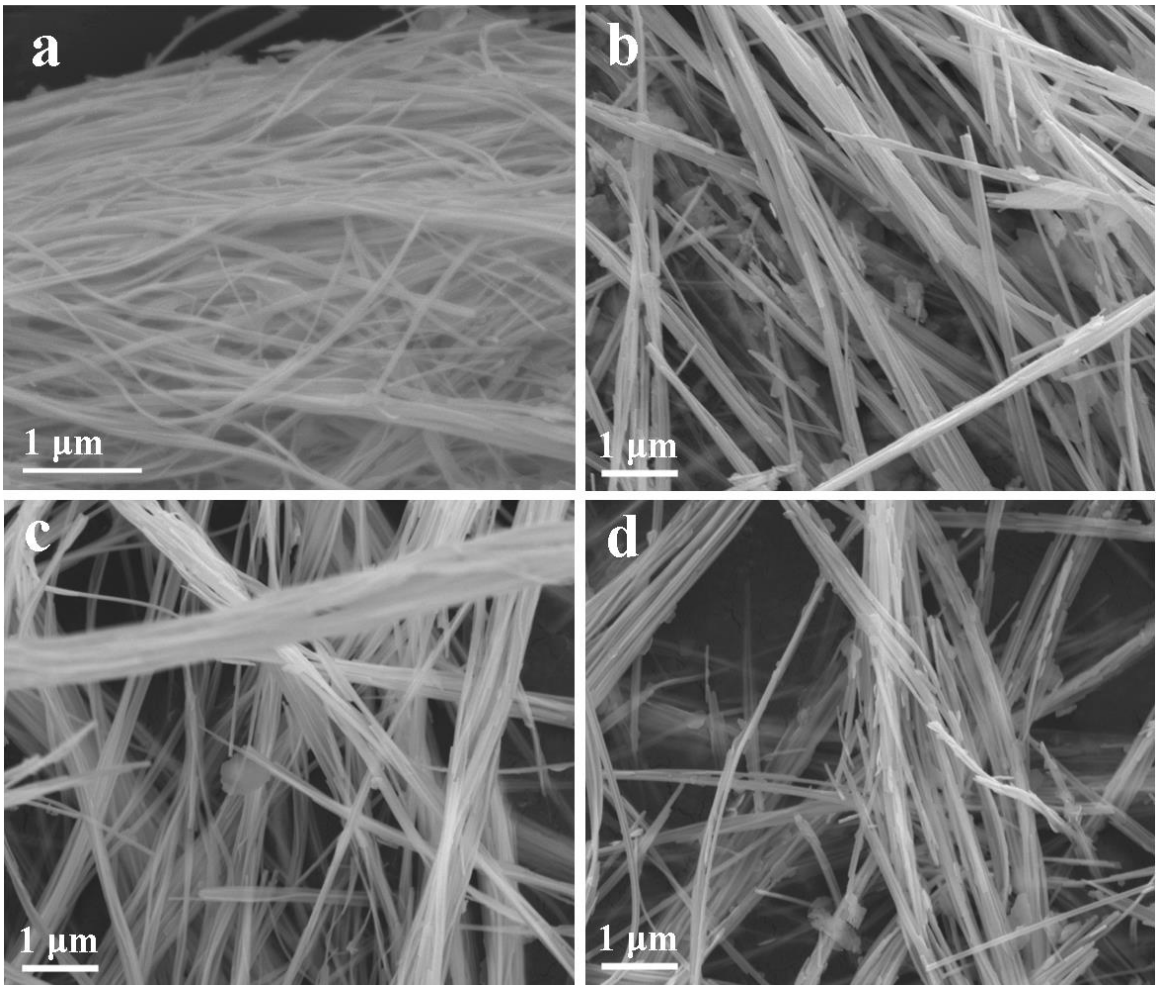

Figure 2. SEM images of (a) pure $(BiO)_2CO_3$ nanowires, (b) Mg^{2+}-doped $(BiO)_2CO_3$ nanowires, (c) Ca^{2+}-doped $(BiO)_2CO_3$ nanowires, and (d) Sr^{2+}-doped $(BiO)_2CO_3$ nanowires

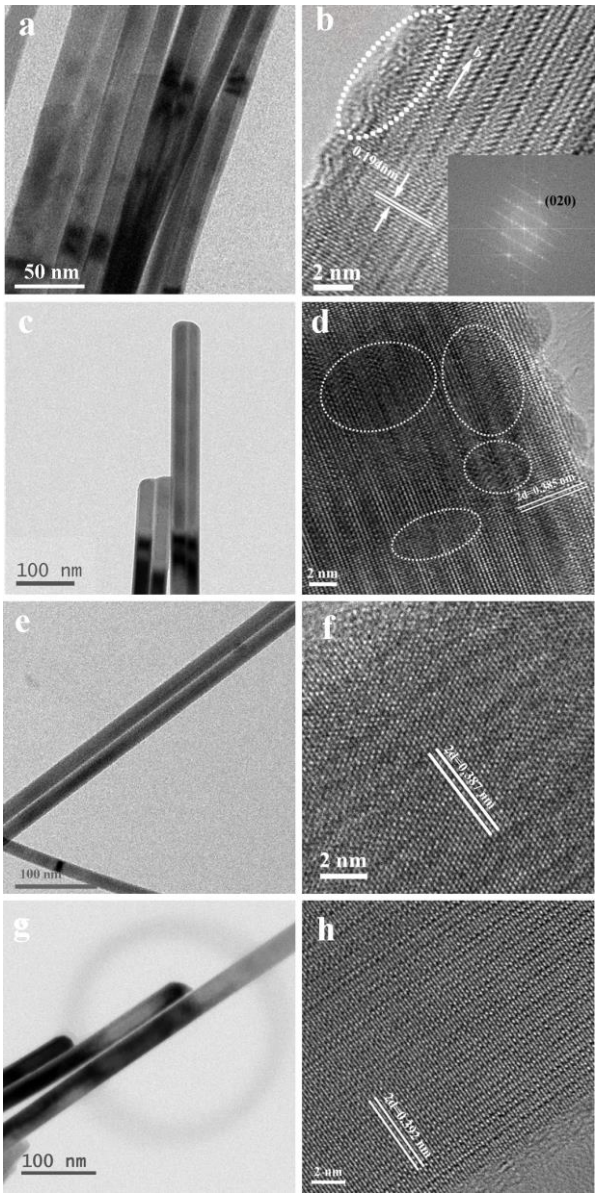

Figure 3. TEM and HRTEM images of (a, b) Pure -doped $(BiO)_2CO_3$ nanowires, (c, d) Mg^{2+}-doped $(BiO)_2CO_3$ nanowires, (e, f) Ca^{2+}-doped $(BiO)_2CO_3$ nanowires, and (g, h) Sr^{2+}-doped $(BiO)_2CO_3$ nanowires

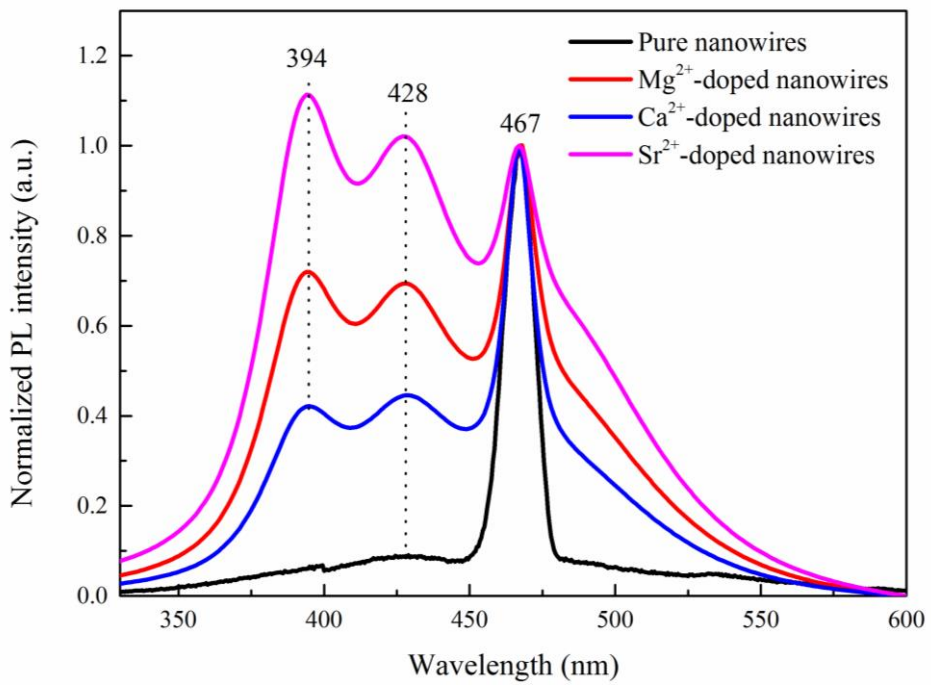

Figure 4. The normalized PL spectra of pure nanowires and doped nanowires

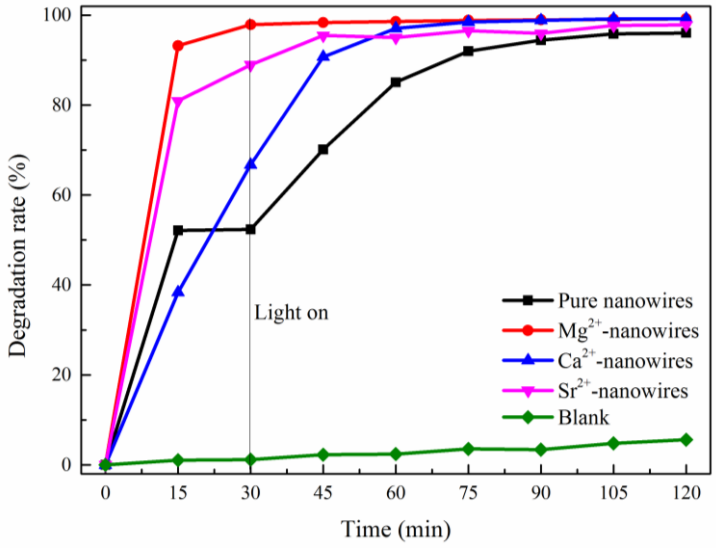

Figure 5. Photocatalytic activity of Mg^{2+}-doped, Ca^{2+}-doped, Sr^{2+}-doped, and pure nanowires for decomposition of xanthate

Table 1. Ion radius ratio, absolute ion radius difference between M^{2+} and Bi^{3+} and lattice constants of pure $(BiO)_2CO_3$ nanowires and $(BiO)_2CO_3$ nanowires doped with Mg^{2+}, Ca^{2+}, or Sr^{2+} ions

	a/ Å	b/ Å	c/ Å	Absolute ion radius difference between M^{2+} and Bi^{3+} /Å	Ion radius ratio of M^{2+}/Bi^{3+}*
Standard values	3.865	3.862	13.675	/	/
Pure $(BiO)_2CO_3$ nanowires	3.868	3.866	13.676	/	/
Mg^{2+}-doped $(BiO)_2CO_3$ nanowires	3.845	3.842	13.396	0.31	0.699
Ca^{2+}-doped $(BiO)_2CO_3$ nanowires	3.848	3.841	13.439	0.03	0.971
Sr^{2+}-doped $(BiO)_2CO_3$ nanowires	3.935	3.846	13.455	0.15	1.140

* M^{2+} denotes Mg^{2+}, Ca^{2+}, and Sr^{2+} ion.

Table 2. PL intensity ratio of different emission of pure nanowires and alkaline-earth metal ions doped nanowires

Doped cation	394 nm (Intrinsic PL) intensity ratio, %	428 nm (Intrinsic defect-induced PL) intensity ratio, %	467 nm (Surface defect-induced PL) intensity ratio, %	482 nm (Impurity defect-induced PL) intensity ratio, %
/	6.84	9.63	83.53	/
Mg^{2+}	23.53	27.44	8.87	40.16
Ca^{2+}	19.10	26.04	14.68	40.18
Sr^{2+}	26.04	29.67	4.91	39.37